ELSEVIER

Thin Solid Films 414 (2002) 136–142

thin solid films

www.elsevier.com/locate/tsf

Exactly solvable model for metal–insulator–metal stepped boundary tunnel junctions

Q.Q. Shu[a,*], Y. Jiang[b], S. Meng[b], G. Lin[b], W.G. Ma[b]

[a]*Department of Materials Science and Technology, School of Science, Shenzhen University, Shenzhen 518060, PR China*
[b]*Department of Modern Physics, University of Science and Technology of China, Hefei 230026, PR China*

Received 3 December 2001; received in revised form 11 April 2002; accepted 12 April 2002

Abstract

An exactly solvable model, which treats the effective barrier potential of the biased metal–insulator–metal tunnel junctions as a trapezoidal potential with an *ideal stepped boundary*, is presented. Thus, the exact analytic expressions for the electron wave functions and the tunneling probabilities were obtained by solving Schrödinger's equation strictly. It is found that if the longitudinal kinetic energy of the electron, E_x, is greater than the shorter side of the trapezoidal potential, in the barrier region Schrödinger's equation has to be solved in the two subregions: where E_x is lower and higher than the barrier height, respectively. In order to compare the ideal stepped boundary model to Brinkman's two approximation models (J. Appl. Phys. 89 (1970) 1915), the graded diffuse boundary and perfectly sharp boundary model, the trapezoidal barrier parameters were determined by fitting the calculated *I–V* curves to the experimental ones at 77 K. The results show that for three types of junctions (with Au, Ag, and Cu top electrodes), the variations in barrier parameters with the metal electrodes are in agreement with each other.

Keywords: Tunneling; Interfaces; Tunnel junctions; Trapezoidal barrier parameters

1. Introduction

Electron transport in metal–insulator–metal (MIM) tunnel junctions is one of the most important tunneling phenomena. The reason for this is that MIM tunnel junctions have been well modeled in studying the electron tunneling through a barrier experimentally and theoretically, and that have been applied in many aspects [1,2]. Recently, due to progress in the investigation of giant magnetoresistance (GMR), the research interests in spin-polarized tunneling magnetoresistance (TMR) of the ferromagnetic MIM tunnel junctions have been increasing rapidly [3,4]. The advantage in research on TMR is that it can be observed at room temperature even without a strong external magnetic field, thus it is a promising GMR device. A key problem in the characterization of the MIM tunnel junctions is to determine their *I–V* characteristics and so far many studies on the calculation of the *I–V* characteristics have been performed [3,4]. Of them, an important work, which was done by Brinkman et al., was to calculate the tunneling conductance of trapezoidal barrier potentials using two extreme models: the *graded diffuse boundary* model and the *perfectly sharp boundary* model [5]. For the graded diffuse boundary model, the tunneling probability was calculated by using the WKB approximation. For the perfectly sharp boundary model, the wave functions were exactly constructed based on the boundary conditions and then the tunneling current is calculated using Bardeen's transfer Hamiltonian method. Brinkman's work has shown that the inclusion of images does not radically alter the shape of the *I–V* characteristics of the junction. It should be emphasized that for the transfer Hamiltonian method the tunneling process is treated as a perturbing operator and then the tunneling matrix elements are calculated. So the transfer Hamiltonian method is a perturbation approximation method and it is effective only for the weak coupling between the wave functions on the two sides of the barrier [1]. In this paper, we will present an *ideal stepped boundary*

*Corresponding author. Tel.: +86-755-653-4023; fax: +86-755-653-4023.
E-mail address: shuqq@szu.edu.cn (Q.Q. Shu).

0040-6090/02/$ - see front matter © 2002 Elsevier Science B.V. All rights reserved.
PII: S0040-6090(02)00455-8

model, which treats the *effective* barrier potential of the biased MIM tunnel junctions as a trapezoidal potential and the resultant barrier potential is the trapezoidal potential plus an applied electric potential resulting from the bias voltage. It means that the applied electric field is located inside the insulator region of the junction and the junctions have the ideal stepped boundaries. Thus, to our knowledge for the first time, the exact analytic expressions for the electron wave functions and the tunneling probabilities in the biased MIM tunnel junctions were obtained by solving Schrödinger's equation strictly, instead of using the WKB approximation or perturbation approximation method. In order to compare our model with Brinkman's graded diffuse boundary model and perfectly sharp boundary model, three groups of the barrier parameters were determined by fitting the calculated I–V curves to the experimental ones for three types of junctions (ones with Au, Ag and Cu top electrodes) at 77 K, respectively. For simplicity, the image force correction is not included because the effect of the image forces is only to round off the barrier corner and to make the average height of the barrier slightly lower [6].

2. Ideal stepped boundary model

Consider a MIM junction consisting of two metal electrodes and separated by a thin barrier insulator layer (10–20 Å). The effective trapezoidal barrier potential of the junction is modeled in one dimension with width d, as shown in Fig. 1a. As the junction is biased, since the applied electric field is located in the insulator region, the resulting barrier potential, $U(x)$, for the biased junction is the barrier potential plus the applied electric potential, as shown in Fig. 1b or c. Based on the free-electron and effective mass approximation, the tunneling electron wavefunctions $\psi(x)$ must satisfy the Schrödinger's equation

$$-\frac{\hbar^2}{2m^*}\frac{\mathrm{d}^2}{\mathrm{d}x^2}\psi(x)+U(x)\psi(x)=E_x\psi(x) \tag{1}$$

where

$$U(x)=\begin{cases}0 & x<0\\ \phi_1+E_{\mathrm{fL}}-(\phi_1-\phi_2+eV)\dfrac{x}{d}, & 0\leqslant x\leqslant d\\ -eV & x>d\end{cases} \tag{2}$$

m^* is the tunneling electron effective mass; E_x is the longitudinal kinetic energy in the x-axis direction (perpendicular to the junction interface). Note that for tunneling problems, there should be $E_x<E_{\mathrm{fL}}+\phi_1$. As seen in Fig. 1a, if the bottom of the conductance band is taken as the zero point of potential, E_{fL} and E_{fR} is the Fermi energy of the left and right electrode, ϕ_1 and ϕ_2 is the trapezoidal barrier height on the left and right; respectively; V is the bias voltage and the electrode on the right is biased positive.

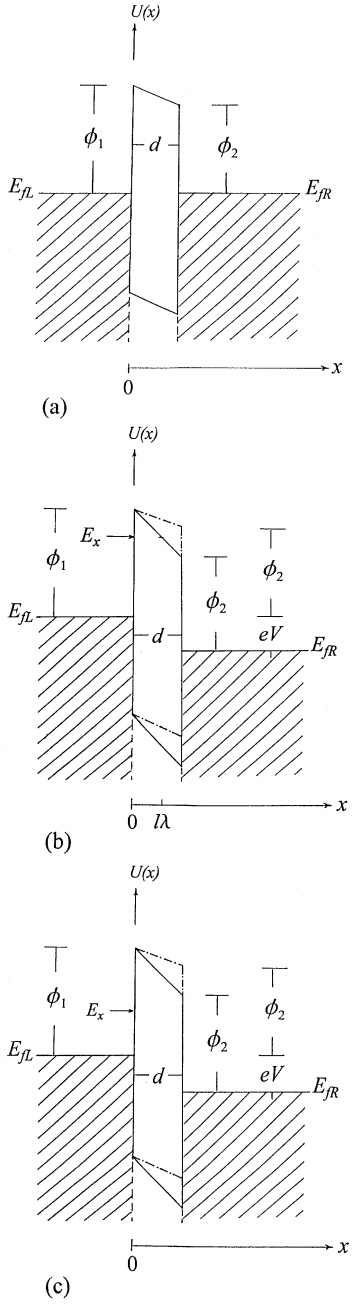

Fig. 1. Trapezoidal potential barrier model of metal–insulator–metal tunnel junctions with (a) zero bias; (b) with a bias positive on the right-hand metal and the electron energy $E_x\geqslant(E_{\mathrm{fL}}+\phi_2-eV)$, i.e. $d\geqslant l\lambda$; and (c) with a bias positive on the right-hand metal and the electron energy $E_x<(E_{\mathrm{fL}}+\phi_2-eV)$, i.e. $d<l\lambda$. The dash–dot lines in (b) and (c) are the barrier potentials with zero bias. Note that for the case of (b), the electron energy $E_x<U(x)$ only in region of $0\leqslant x\leqslant l\lambda$.

In the region $x<0$ and $x>d$, the solutions for Eq. (1) has, respectively, the form of $\psi_1(x)$ and $\psi_4(x)$

$$\psi_1(x)=e^{ik_{1x}}+Re^{-ik_{1x}}, \qquad x<0 \tag{3}$$

$$\psi_4(x)=Se^{ik_{2x}}, \qquad x>d \tag{4}$$

where R and S is the reflection and transmission coefficient, respectively; $k_1=(2m^*E_x)^{1/2}/\hbar$, $k_2=[2m^*(E_x+eV)]^{1/2}/\hbar$.

In the barrier region $0\leqslant x\leqslant d$, by introducing

$$l=\left[\frac{d\hbar^2}{2m^*(\phi_1-\phi_2+eV)}\right]^{1/3} \tag{5a}$$

$$\lambda=\frac{2m^*(\phi_1+E_{fL}-E_x)l^2}{\hbar^2} \tag{5b}$$

Eq. (1) becomes

$$\frac{d^2\psi}{dx^2}+\left(\frac{x}{l^3}-\frac{\lambda}{l^2}\right)\psi=0 \tag{6}$$

Both l and λ are positive, l has a length dimension and λ is dimensionless. Note that because the tunneling electrons with the different E_x face different parts of the trapezoidal barrier, in solving Eq. (6) there are two cases to be considered separately: $l\geqslant\lambda$, i.e. $E_x\geqslant(E_{fL}+\phi_2-eV)$ and $l<\lambda$, i.e. $E_x<(E_{fL}+\phi_2-eV)$.

As shown in Fig. 1b, in the case of $d\geqslant l\lambda$ for the tunneling electron there are the two different subregions inside the trapezoidal barrier region: $0\leqslant x<l\lambda$ (E_x is *lower* than the barrier potential) and $l\lambda\leqslant x\leqslant d$ (E_x is *higher* than the barrier potential).

In the barrier subregion $0\leqslant x<l\lambda$ (E_x is lower than the barrier potential), introducing the dimensionless parameter $\xi=\lambda-(x/l)$, Eq. (6) becomes

$$\frac{d^2\psi}{d\xi^2}+\xi\psi=0 \tag{7}$$

In terms of the transformations and $z=(2/3)\xi^{3/2}$, Eq. (7) can be rewritten as

$$\frac{d^2\varphi}{dz^2}+\frac{1}{z}\frac{d\varphi}{dz}-\left[1+\frac{(1/3)^2}{z^2}\right]\varphi=0, \quad \text{for } 0\leqslant x<l\lambda \tag{8a}$$

This is a modified Bessel equation, a general solution of which is

$$\varphi(x)=C_1I_{1/3}(z)+C_2K_{1/3}(z) \tag{8b}$$

where $I_{1/3}$ and $K_{1/3}$ are modified Bessel functions [7].

Similary, in the barrier *subregion* $l\lambda\leqslant x\leqslant d$ (E_x is higher than the barrier potential), introducing $\xi=(x/l)-\lambda$, Eq. (6) is rewritten as $d^2\psi/d\psi^2+\xi\psi=0$, which can be transformed, by using $\psi=\xi^{1/2}\varphi$ and $z=(2/3)\xi^{3/2}$, as a Bessel equation of one third order

$$\frac{d^2\varphi}{dz^2}+\frac{1}{z}\frac{d\varphi}{dz}+\left[1-\frac{(1/3)^2}{z^2}\right]\varphi=0, \quad \text{for } l\lambda\leqslant x\leqslant d \tag{9a}$$

a general solution of which is

$$\varphi(x)=D_1J_{1/3}(z)+D_2N_{1/3}(z) \tag{9b}$$

where $J_{1/3}$ is Bessel function, $N_{1/3}$ is Neumann function [7].

Thus, for the case of $d\geqslant l\lambda$, returning to the variable x in Eq. (8b) and Eq. (9b), we obtained the solutions of Eq. (6), ψ_2 and ψ_3 as follows:

$$\psi_2(x)=\left(\lambda-\frac{x}{l}\right)^{1/2}\left\{C_1I_{1/3}\left[\frac{2}{3}\left(\lambda-\frac{x}{l}\right)^{3/2}\right]+C_2K_{1/3}\left[\frac{2}{3}\left(\lambda-\frac{x}{l}\right)^{3/2}\right]\right\}, \quad 0\leqslant x\leqslant l\lambda \tag{10}$$

$$\psi_3(x)=\left(\frac{x}{l}-\lambda\right)^{1/2}\left\{D_1J_{1/3}\left[\frac{2}{3}\left(\frac{x}{l}-\lambda\right)^{3/2}\right]+D_2N_{1/3}\left[\frac{2}{3}\left(\frac{x}{l}-\lambda\right)^{3/2}\right]\right\}, \quad l\lambda\leqslant x\leqslant d \tag{11}$$

where C_1, C_2, D_1 and D_2 are unknown constants. Using (i) the recurrence relations of Bessel, Neumann and modified Bessel functions [7], and (ii) the boundary conditions at $x=0$, $l\lambda$ and d: $\psi_1(0)=\psi_2(0)$ and $\psi'_1(0)=\psi'_2(0)$; $\psi_2(l\lambda)=\psi_3(l\lambda)$ and $\psi'_2(l\lambda)=\psi'_3(l\lambda)$; $\psi_3(d)=\psi_4(d)$ and $\psi'_3(d)=\psi'_4(d)$, the constant C_1, C_2, C_1 and D_2, along with R and S in Eq. (3) and Eq. (4), were determined as follows:

$$C_1=\frac{2ik_1-b_{24}C_2\pi/2\sin(\pi/3)}{b_{13}},$$

$$C_2=\frac{4ik_1\sin(\pi/3)}{b_{24}\pi+b_{13}\pi[-(b_{68}/b_{57})+1+\cos(\pi/3)]},$$

$$D_1=\frac{b_{68}C_2\pi}{2b_{57}\sin(\pi/3)},\ D_2=-C_2\pi/2,$$

$$R=C_1a_1+\frac{a_2C_2\pi}{2\sin(\pi/3)}-1,$$

$$S=e^{-ik_2d}[a_5D_1+a_6D_2/\sin(\pi/3)] \tag{12}$$

where $b_{13}=ik_1a_1-a_3/2$, $b_{24}=ik_1a_2-a_4/2$, $b_{57}=ik_2a_5-a_7/2$, $b_{68}=ik_2a_6-a_8/2$ and

$$a_1=\lambda^{1/2}e^{-i\pi/6}J_{1/3}(t_0),\ a_2=\lambda^{1/2}[e^{i\pi/6}J_{-1/3}(t_0)-e^{-i\pi/6}J_{1/3}(t_0)],$$

$$a_3=\frac{1}{l\lambda^{1/2}}e^{-i\pi/6}J_{1/3}(t_0)+\frac{\lambda}{l}e^{i\pi/3}[J_{-2/3}(t_0)-J_{4/3}(t_0)],$$

$$a_4=\frac{1}{l\lambda^{1/2}}[e^{i\pi/6}J_{-1/3}(t_0)-e^{-i\pi/6}J_{1/3}(t_0)]+\frac{\lambda}{l}\times\{e^{i2\pi/3}[J_{-4/3}(t_0)-J_{2/3}(t_0)]-e^{i\pi/3}[J_{-2/3}(t_0)-J_{4/3}(t_0)]\},$$

$$a_5=(d/l-\lambda)^{1/2}J_{1/3}(t_1)$$

$$a_6=(d/l-\lambda)^{1/2}[J_{1/3}(t_1)\cos(\pi/3)-J_{-1/3}(t_1)],$$
$$a_7=\frac{1}{l(d/l-\lambda)^{1/2}}J_{1/3}(t_1)+\frac{(d/l-\lambda)}{l}[J_{-2/3}(t_1)-J_{4/3}(t_1)],$$
$$a_8=\frac{1}{l(d/l-\lambda)^{1/2}}[J_{1/3}(t_1)\cos(\pi/3)-J_{-1/3}(t_1)]+\frac{(d/l-\lambda)}{l}\{[J_{-2/3}(t_1)-J_{4/3}(t_1)]\cos(\pi/3)-[J_{-4/3}(t_1)-J_{2/3}(t_1)]\}$$

and $t_0=\frac{2}{3}\lambda^{3/2}e^{i\pi/2}$ and $t_1=\frac{2}{3}(d/l-\lambda)^{3/2}$.

As shown in Fig. 1c, in the case of $d<l\lambda$, over all the barrier region E_x is lower than the barrier potential and thus the wave functions of the tunneling electron must only satisfy Eq. (8a) and there are the constant R, S, C_1, C_2 to be determined. In this case, the solutions of Eq. (8a) has the form of Eq. (10) in the region $0\leqslant x\leqslant d$ instead of the region $0\leqslant x\leqslant l\lambda$. Using the boundary conditions at $x=0$ and $x=d$: $\psi_1(0)=\psi_2(0)$ and $\psi'_1(0)=\psi'_2(0)$; $\psi_2(d)=\psi_4(d)$ and $\psi'_2(d)=\psi'_4(d)$, the constant C_1, C_2, R and S were determined as follows:

$$C_1=\frac{2ib_{68}k_1}{b_{13}b_{68}-b_{57}b_{24}},$$
$$C_2=\frac{2b_{57}C_1\sin(\pi/3)}{b_{68}\pi},$$
$$R=C_1a_1+\frac{a_2C_2\pi}{2\sin(\pi/3)}-1,$$
$$S=e^{-ik_2d}[a_5C_1+a_6C_2\pi/2\sin(\pi/3)] \quad (13)$$

where $b_{57}=ik_2a_5+a_7/2$, $b_{68}=ik_2a_6+a_8/2$, and

$$a_5=(\lambda-d/l)^{1/2}e^{-i\pi/6}J_{1/3}(t_1),$$
$$a_6=(\lambda-d/l)^{1/2}[e^{i\pi/6}J_{-1/3}(t_1)-e^{-i\pi/6}J_{1/3}(t_1)],$$
$$a_7=\frac{1}{l(\lambda-d/l)^{1/2}}e^{-i\pi/6},J_{1/3}(t_1)+\frac{(\lambda-d/l)}{l}e^{i\pi/3}[J_{-2/3}(t_1)-J_{4/3}(t_1)],$$
$$a_8=\frac{1}{l(\lambda-d/l)^{1/2}}[e^{i\pi/6}J_{-1/3}(t_1)-e^{-i\pi/3}J_{1/3}(t_1)]+\frac{(\lambda-d/l)}{l}\{e^{i2\pi/3}[J_{-4/3}(t_1)-J_{2/3}(t_1)]-e^{i\pi/6}[J_{-2/3}(t_1)-J_{4/3}(t_1)]\}$$

and $t_1=\frac{2}{3}(\lambda-d/l)e^{i\pi/2}$.

We have obtained the exact analytic solutions (for the electron wave functions) of Eq. (1) in the two cases: (i) $d\geqslant l\lambda$, the solutions consist of Eq. (3), Eq. (4), Eq. (10), Eq. (11) and Eq. (12); (ii) $d<l\lambda$, the solutions consist of Eq. (3), Eq. (4), Eq. (10) and Eq. (13). The electron tunneling probability, P, is given by

$$P=|S^2| \quad (14)$$

where S is the transmission coefficient appearing in Eq. (4). The tunneling current density is [8]

$$\begin{aligned}J&=\frac{4\pi em^*}{h}\int_0^{E_{x\mathrm{MAX}}}|S|^2dE_x\int_0^{\infty}[f_L(E_x+E_r)-f_R(E_x+E_reV)]dE_r\\&=\frac{4\pi em^*}{h}\int_0^{E_{x\mathrm{MAX}}}|S|^2k_BT\left[\ln\frac{e^{E_r/k_BT}}{1+e^{E_r/k_BT}e^{(E_x-E_{fL})/k_BT}}-\ln\frac{e^{E_r/k_BT}}{1+e^{E_r/k_BT}e^{(E_x-E_{fR}+eV)/k_BT}}\right]_{E_r=0}^{E_r=\infty}dE_x\\&=\frac{4\pi em^*}{h}\int_0^{E_{x\mathrm{MAX}}}|S|^2k_BT\times\left[\frac{eV}{k_BT}-\ln\frac{1+e^{(E_x-E_{fL})/k_BT}}{1+e^{(E_x-E_{fR}+eV)/k_BT}}\right]dE_x\end{aligned} \quad (15)$$

where $E_r=E-E_x$ is the transverse kinetic energy of the electron in the direction perpendicular to the x-axis (parallel to the junction interface), k_B is Boltzmann's constant and T is temperature.

3. Experiment

In order to compare Brinkman's two extreme models to the ideal stepped boundary model presented in this paper, we determined the parameters (width and height) of the trapezoidal effective barrier by fitting the calculated I–V curves based on the above the three models to the experimental ones. The preparation of the junctions used to obtain the experimental I–V curves was described in detail elsewhere [9]. First, Al film strips were evaporated on glass slides in a vacuum chamber of typically 2×10^{-5} Torr. Then, to grow a thin Al_2O_3 barrier layer on the Al film surface, the Al films were exposed to an oxygen glow discharge at the pressure of 1×10^{-1} Torr for 10 min. This was followed by baking the samples in air at 200 °C for 30 min and then cooling the heated samples in air to room temperature slowly. Next MgF_2 film strips were evaporated over the edges of the oxidized Al film strips to increase the insulator thickness at the edges. Finally, the top metal electrode film strips (Au, Ag, or Cu) were deposited and the tunnel junctions of 2.5×2.5 mm^2 were obtained. Baking the samples in air made the Al_2O_3 barrier layer denser and the increase in the insulator thickness at the edges eliminated the problem of leakage current at the junction edges, thus the applied bias to the junctions can be up to 5.12 V at room temperature. The experimental I–V curves of the junctions are shown in Fig. 2 and were measured in a liquid nitrogen Dewar (77 K) and the top metal electrodes on the right were biased positively.

The bare Al_2O_3 barrier layer thickness was measured with an ellipsometer (Rudolph 2436) before the top metal electrode deposition. The incident angle of the

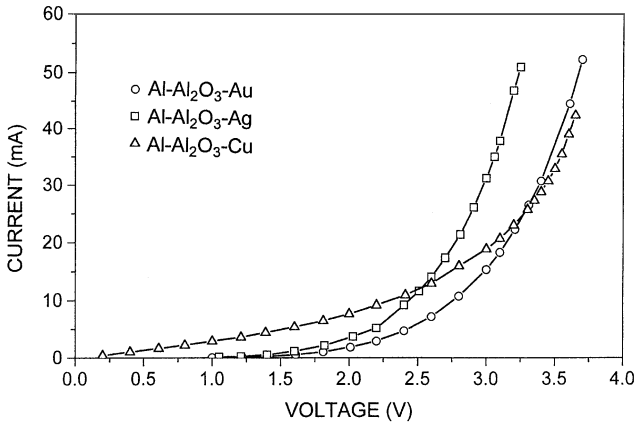

Fig. 2. The experimental I–V characteristics of the tunnel junctions at 77 K.

light beam to the bare Al_2O_3 barrier layer was 70° and the wavelength was 5461 Å. Care should be taken to choose the complex optical constant of the Al film on which the Al_2O_3 barrier layer was grown. The reason for this is that the complex optical constant of the evaporated Al films depends on the deposition conditions.

4. Results and discussion

For thermal equilibrium the Fermi energy levels of a system of metal electrodes in the tunnel junctions must be in coincidence, hence in the case of metal electrodes the vacuum level also must be in coincidence. Since the Al bottom electrode (on the left in Fig. 1) was always biased negatively, in order to simplify the calculation of the theoretical I–V curves, we did not distinguish between the left- and right-hand electrodes in Eq. (15) and took the Fermi energy levels for both electrodes to be 11.63 eV (i.e. the Fermi energy of Al). The reason for this is that: (i) the selection of which electrode to use is basically immaterial from the point of view of reflecting structure in the tunneling conductance [5,8]; (ii) the effect of two dissimilar electrodes in the MIM tunnel junctions is to produce two unequal barrier heights at two interfaces between each electrodes and the insulating barrier film, and it has been included in the trapezoidal barrier potential model [6]. The effective mass of electron in the Al_2O_3 barrier layer, m^*, was chosen to be 0.2 m_e, where m_e is the free-electron mass [9]. Thus, the barrier parameters obtained by fitting the calculated I–V curves to the experimental ones are shown in Table 1.

The bare Al_2O_3 barrier layer thickness was determined to be 34.2 ± 2.5 Å by the ellipsometric measurement and it is greater than the barrier width d, as shown in Table 1. This difference can be understood as follows: (i) because grown Al_2O_3 barrier layer is not uniform and has the surface roughness, and the tunneling probability increases exponentially with decrease in the barrier width, the tunneling electrons prefer to go through the thinner area. Since the ellipsometric values are the geometric average ones, the tunneling values are the physical effective ones; (ii) the diffusion of the metal electrode atoms into the barrier layer leads to a decrease in the average barrier thickness.

As seen in Table 1, for the ideal stepped boundary model the barrier height ϕ_1 in the Au- (Ag-, Cu-) junctions are approximately equal to each other because they characterizes the same Al–Al_2O_3 interface. The results for the ideal stepped boundary model are what they should be and are in agreement with ones for both graded diffuse boundary and perfectly sharp boundary models. In contrast, for all the three models the barrier height ϕ_2 at the Al_2O_3–Au (–Ag, –Cu) interface are quite different, in particular, ϕ_2 at the Al_2O_3–Cu interface much higher than that at the Al_2O_3–Au (–Ag) interface.

For both graded diffuse boundary and perfectly sharp boundary models, the difference in the barrier height ϕ_2 between the Al_2O_3–Au (–Ag) and –Cu interfaces can be understood by considering that at the interfaces oxygen atoms with dangling bonds can combine with Cu atoms but inactive Au and Ag atoms, thus copper oxide of one or two monolayer thickness is grown at the interface and an additional barrier must be considered [10]. On the other hand, the top electrode atoms have the different atom radii: 1.439 Å (Au), 1442 Å (Ag), 1.280 Å (Cu) and the Cu atoms with the smaller radium are easier to diffuse into the Al_2O_3 barrier. As shown in Table 1, this means that the barrier width of

Table 1
The effective trapezoidal barrier parameters determines by fitting the calculated I–V curves to the experimental ones

Parameters / Models	d (Å)			ϕ_1 (eV)			ϕ_2 (eV)		
	GDB	PSB	ISB	GDB	PSB	ISB	GDB	PSB	ISB
Al–Al_2O_3–Au	24.4	27.3	21.0	2.65	3.25	4.07	1.05	0.95	1.82
Al–Al_2O_3–Ag	25.3	28.0	23.1	2.90	3.40	3.77	0.85	0.90	1.77
Al–Al_2O_3–Cu	12.0	10.7	15.2	2.85	2.95	3.78	3.10	3.30	2.97

The calculated I–V curves were in the basis of Brinkmann's graded diffuse boundary (GDB) model and perfectly sharp boundary (PSB) model, and the ideal stepped boundary (ISB) model presented in this paper.

the Cu-junction is much shorter than that of the Au- and Ag-junctions. However, for inelastic electron tunneling spectroscopy (IETS) the case is different. It is found that some top metal electrodes of junctions (e.g. Al and Cr) will destroy the layer of molecules that were doped into the junction and others (e.g. Pb and Ti) will not [11]. For Pb top electrode, tunneling spectra are obtained that closely resemble infrared spectra or Raman spectra of the dopant molecules without a top electrode. Therefore, Pb top electrode is widely used in junctions of IETS.

Based on the same explanations as above, for the ideal stepped boundary model the ϕ_2 at the Al_2O_3–Cu interface much higher than that at the Al_2O_3–Au (–Ag) interface and the barrier width of the Cu-junction is much shorter than that of the Au- and Ag-junctions. It should be noted that, as seen in Table 1, in the Cu-junction there is $\phi_1 < \phi_2$ for both graded diffuse boundary and perfectly sharp boundary models and, in contrast, there is $\phi_1 > \phi_2$ for the ideal stepped boundary model. This difference between the ideal stepped boundary model and the graded diffuse (or the perfectly sharp) boundary model can be explained as follows: as seen in Eq. (5a), l (with a length dimension) should be positive for any given bias voltage V, in other words, for the ideal stepped boundary model the assumption of $\phi_1 > \phi_2$ has been made (of course, the another assumption of $\phi_1 < \phi_2$ can be chosen to make). In contrast, for the graded diffuse (or the perfectly sharp) boundary model there is not such a pre-assumption of $\phi_1 > \phi_2$ (or $\phi_1 < \phi_2$). It should be emphasized that the assumption of $\phi_1 > \phi_2$ makes no difference to characterizing the junction interfaces. For example, as shown in Table 1, for the ideal stepped boundary model the barrier height $\phi_2 = 1.82$, 1.77 and 2.97 eV at the Al_2O_3–Au, –Ag and –Cu interface, respectively, and the ϕ_2 at the Al_2O_3–Cu interface are much higher than that at the Al_2O_3–Au (–Ag) interface. Obviously, for ideal stepped boundary model the variation in the ϕ_2 values with the top electrodes is in agreement with that for the graded diffuse boundary model and the perfectly sharp boundary model.

The experimental I–V curves were measured at in liquid nitrogen (77 K), which is easy to get. The temperature dependence of the current density in a MIM tunnel junction can be described by $J(V,T) = J(V,0)[1 + (\pi c_1 k_B T)^2(1/6) + (\pi c_1 k_B T)^4(7/360) + \cdots]$, where V is the bias voltage, T is temperature, k_B is Boltzmann constant and the coefficient c_1 for small bias voltages ($\leqslant 1.0$ V) is approximately 20 $(\mathrm{eV})^{-1}$ [12]. Since $k_B T$ (77 K) $= 64 \times 10^{-3}$ eV, the increase in the current density is less 3% as the temperature goes from 0 to 77 K. This shows that the I–V characteristics at 77 K differs only slightly from that at 4.2 K. Recently, temperature dependence of the (spin-independent) conductance G (T, $V = 0$) for a zero-biased Co–insulator–Py tunnel junction with the insulator composed of 4 Å Al and 10 Å Dy oxidized was measured, but the temperature dependence of the I–V characteristics is absent from this type of tunnel junction [13]. In general, a small influence of temperature on the I–V characteristics is typical for tunneling. Nevertheless, there is still a requirement for measuring the temperature dependence of the I–V characteristics, in particular, for determining the temperature dependence of the tunneling barrier parameters. It would be good to perform the measurements of the I–V characteristics at a temperature as low as possible to eliminate thermionic emission, which will results in a nontunneling current component in the junctions. However, for IETS the tunneling spectra are taken always at 4.2 K (or lower temperature). The reason for this is that vibrational modes of surface species have characteristic width of order 1 meV (or greater) and a contribution to the spectrum width is made by the thermal broadening, which comes from the thermal smearing of the electron distribution around the Fermi energy [11]. Hence, the tunneling spectra must be run at cryogenic temperature to obtain resolutions sufficient for the vibrational spectroscopy.

5. Summary

We presented an ideal stepped boundary model, which treats the effective barrier potential of the biased MIM tunnel junctions as a trapezoidal potential plus an applied electric potential (from the biased voltage). Thus, to our knowledge for the first time, the exact analytic expressions for the electron wave functions and the tunneling probabilities were obtained by solving Schrödinger's equation strictly. For comparison to Brinkman's two extreme models: the graded diffuse boundary model (based on WKB approximation) and the perfectly sharp boundary model (based on perturbation approximation), the three groups of barrier parameters were determined by fitting the calculated I–V curves to the experimental ones for three different junctions with the Au, Ag and Cu top electrodes at 77 K. The results show that: (i) according to the ideal stepped boundary model the tunneling electron behavior in the trapezoidal barrier region is dependent on whether the electron energy E_x is lower or higher than the barrier height; (ii) the variations in the barrier parameters obtained from the above three models are in qualitative agreement with each other. Also the results suggest that though a barrier layer of tunnel junctions is a real existence, it can be modeled in many ways to different effective barrier potentials, for example, to rectangular or trapezoidal ones with diffuse or sharp boundaries. Thus, a group of the barrier parameters for each effective barrier potential model can be obtained by fitting the calculated I–V curves based on the barrier model to the experimental

ones. In addition, since the ferromagnetic MIM tunnel junctions with TMR is a promising GMR device, the effect of an applied external magnetic field on the calculated barrier parameters on the basis of our model should be a forthcoming subject for study.

Acknowledgments

This work was supported by Research and Development Programs of Shenzhen.

References

[1] E.L. Wolf, Principles of Electron Tunneling Spectroscopy, Oxford University Press, New York, 1985, p. 36.
[2] R. Wiesendanger, Spin-polarized scanning tunneling microscopy, in: R. Wiesendanger (Ed.), Scanning Probe Microscopy, Springer, Berlin, 1998, p. 71.
[3] J.S. Moodera, J. Nowak, R.J.M. van de Veerdonk, Phys. Rev. Lett. 80 (1998) 2941.
[4] Z. Zhang, S. Cardoso, P.P. Freitas, X. Batlle, P. Wei, N. Barradas, J.C. Soares, J. Appl. Phys. 89 (2001) 6665.
[5] W.F. Brinkman, R.C. Dynes, J.M. Rowell, J. Appl. Phys. 41 (1970) 1915.
[6] J.G. Simmons, J. Appl Phys. 34 (1963) 2581.
[7] G. Arfken, Mathematical Methods for Physicists, second ed., American Press, New York, 1970, p. 478.
[8] C.B. Duke, Theory of metal–barrier–metal tunneling, in: E. Burstein (Ed.), Tunneling Phenomena in Solids, Plenum, New York, 1969, p. 31.
[9] Q.Q. Shu, W.G. Ma, Appl. Phys. Lett. 61 (1992) 2524.
[10] D.G. Walmsley, R.B. Floyd, W.E. Timms, Solid State Commun. 22 (1977) 497.
[11] P.K. Hansma, Introduction, in: P.K. Hansma (Ed.), Tunneling Spectroscopy, Plenum Press, New York, 1982, p. 1.
[12] T.E. Hartman, J.S. Chivian, Phys. Rev. 134 (1964) A1094.
[13] C.H. de Groot, Y. Ouyang, Sang-Mo Koo, E. Kendall, Q.Q. Shu, J.S. Moodera, J. Phys.: Condens. Matter 14 (2002) 5153.